The impact of P(NDI2OD-T2) crystalline domains on the open-circuit voltage of bilayer all-polymer solar cells with an inverted configuration

Yu Jin Kim and Chan Eon Park

Articles you may be interested in

Quadruple-junction thin-film silicon-based solar cells with high open-circuit voltage
Appl. Phys. Lett. **105**, 063902 (2014); 10.1063/1.4892890

Increased open-circuit voltage in bulk-heterojunction solar cells using a C 60 derivative
Appl. Phys. Lett. **97**, 193309 (2010); 10.1063/1.3518066

Device physics of inverted all-polymer solar cells
J. Appl. Phys. **107**, 114501 (2010); 10.1063/1.3371364

Enhanced open-circuit voltage in polymer solar cells
Appl. Phys. Lett. **95**, 043301 (2009); 10.1063/1.3157278

Cathode dependence of the open-circuit voltage of polymer:fullerene bulk heterojunction solar cells
J. Appl. Phys. **94**, 6849 (2003); 10.1063/1.1620683

The impact of P(NDI2OD-T2) crystalline domains on the open-circuit voltage of bilayer all-polymer solar cells with an inverted configuration

Yu Jin Kim and Chan Eon Park[a]
POSTECH Organic Electronics Laboratory, Department of Chemical Engineering,
Pohang University of Science and Technology, Pohang 790-784, South Korea

We fabricated P(NDI2OD-T2)/PTB7 bilayer all-polymer solar cells with an inverted configuration, where the annealing temperature was systematically varied. The current density–voltage behavior was investigated and the structural properties of the P(NDI2OD-T2) layers were characterized. Absorption spectroscopy, surface morphology, and crystallite analysis showed that increasing phase segregation of P(NDI2OD-T2) films occurred as the annealing temperature increased. We found that, as the P(NDI2OD-T2) stacking improved, with larger domains, the open-circuit voltage decreased and the saturation dark current density increased. This work provides a guide for the processing of P(NDI2OD-T2) layers to maximize the power conversion efficiency of all-polymer solar cells. © *2015 Author(s). All article content, except where otherwise noted, is licensed under a Creative Commons Attribution 3.0 Unported License.* [http://dx.doi.org/10.1063/1.4937469]

All-polymer solar cells (APSCs) consisting of binary blends of conjugated donor and acceptor polymers have attracted much recent research interest, primarily owing to the following advantages over polymer/fullerene solar cells: (1) effective tuning of the optical, electronic, and morphological characteristics; (2) potential to convert a large portion of sunlight in the visible and near-infrared wavelengths; and (3) favorable mechanical and thermal properties.[1–4] Despite these advantages, to date, APSCs have exhibited relatively low power conversion efficiencies of only 4%–6%,[3,5,6] which is significantly lower than have been achieved using polymer/fullerene systems (9%–10%).[7,8] To develop improved all-polymer blend systems, a fundamental understanding of the critical factors determining the device performance is required.

One of the most important parameters affecting the overall performance of organic solar cells is the open-circuit voltage, V_{oc}. Several factors affect V_{oc}, including the energy difference of the donor/acceptor material combination, the sunlight intensity, the type of electrodes, and the device operating temperature.[9–11] Several studies have reported dependences of V_{oc} on the morphological and structural properties. Thompson *et al.* reported that, by using donor materials that inhibit intermolecular π–π interactions, they were able to decrease the saturation dark current density, leading to a high V_{oc}.[12] O'Connor *et al.* used a similar approach with poly(3-hexylthiophene-2,5-diyl) (P3HT) to increase V_{oc} by controlling the stacking of P3HT molecules.[13] A more thorough understanding of the way the molecular structure influences V_{oc} is expected to aid the development of new structures with improved V_{oc}.

In this work, we report on the changes in V_{oc} in APSCs formed with an inverted acceptor polymer/donor polymer structure as a function of the annealing temperature, which affects the morphology. In particular, we explore the relationship between the reverse saturation current and V_{oc}, as well as the effects of the crystal morphology on the magnitude of the reverse saturation current. To control the morphological characteristics, we varied the annealing temperature used during the formation

---

[a]Author to whom correspondence should be addressed. Electronic mail: cep@postech.ac.kr
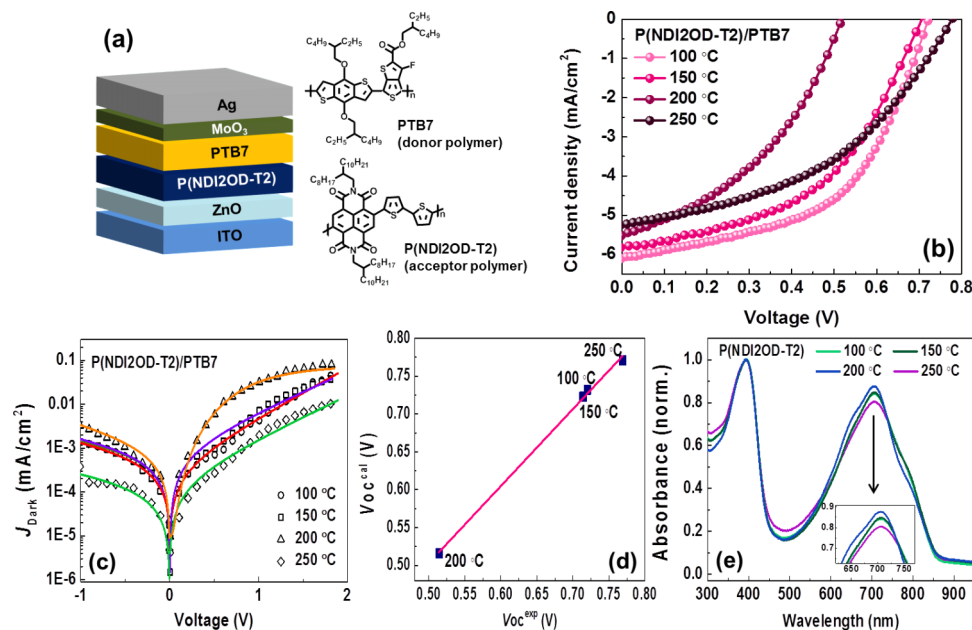
     3, 126105-1

FIG. 1. Inverted P(NDI2OD-T2)/PTB7 bilayer solar cells annealed at different temperatures. (a) The device architecture and molecular structures of P(NDI2OD-T2) and PTB7. (b) The $J-V$ characteristics under illumination, (c) the $J-V$ curves measured in the dark, and (d) the correlation between the experimental V_{oc} ($V_{oc}{}^{exp}$) and calculated V_{oc} ($V_{oc}{}^{cal}$). (e) Normalized UV-vis absorption spectra of the P(NDI2OD-T2) films annealed at different temperatures.

of the bottom polymer layer, which altered the molecular stacking. We used the following two active layers: poly{[N,N-9bis(2-octyldodecyl)-naphthalene-1,4,5,8-bis(dicarboximide)-2,6-diyl]alt-5,59-(2,29-bithiophene)}(P(NDI2OD-T2)) as the acceptor layer and poly{[4,8-bis[(2-ethylhexyl) oxyl]benzo[1,2-b:4,5-b′]dithiophene-2,6-diyl][3-fluoro-2-[(2-ethylhexyl)carbonyl]thieno[3,4-b]thio phenediyl]}(PTB7) as the donor layer. Figure 1(a) shows the device geometry and the molecular structures. To the best of our knowledge, there have been no prior reports of the use of P(NDI2OD-T2) and PTB7 together in bilayer inverted APSCs. Here, we systematically varied the annealing temperature to alter the structural properties of the P(NDI2OD-T2) layer. Our work represents a significant advance in the understanding of the relationships between V_{oc} and morphological factors in APSCs.

The all-polymer bilayer solar cells were fabricated on patterned indium tin oxide (ITO) glass substrates, with an inverted ITO/ZnO/P(NDI2OD-T2)/PTB7/MoO$_3$/Ag structure. The ITO-coated glass substrates were first cleaned in an ultrasonic bath using detergent, deionized water, acetone, and isopropyl alcohol, followed by ultraviolet (UV)–ozone treatment for 20 min. To form the hole-blocking layer, a ZnO film was prepared using a sol–gel process, as described by Heeger *et al.*[14] The ZnO sol-gel was spin-coated on the cleaned ITO-coated glass substrates at 3000 rpm, and the resulting ZnO films were annealed at 200 °C for 1 h in air. A 30-mg/ml solution of P(NDI2OD-T2) (1-Materials, Inc., with a molecular weight of M_w = 174 000 g mol^{-1}) was dissolved in chlorobenzene for 1 h and then spin-coated onto the ZnO layer at 1000 rpm for 30 s. The bottom P(NDI2OD-T2) layers were annealed at 100 °C, 150 °C, 200 °C, or 250 °C for 15 min in an N$_2$ environment. A solution of PTB7 (1-Materials, Inc., M_w = 174 000 g mol^{-1}) was prepared in dichloromethane and deposited onto the P(NDI2OD-T2) layer using spin-coating at 1200 rpm for 20 s. Finally, a 5-nm-thick MoO$_3$ layer and a 100-nm-thick Ag layer were deposited sequentially using vacuum thermal evaporation at 2×10^{-6} Torr.

The current density–voltage ($J-V$) characteristics of the devices were measured using a Keithley 2400 parameter analyzer, both in the dark and under a simulated solar spectrum (AM 1.5G) with an intensity of 100 mW/cm^2. Masks with a well-defined area of 9 mm^2 were used to provide accurate measurements. The solar cells were tested under various light intensities by modulating the intensity of the light with a series of two neutral density filter wheels with six

filters each, allowing up to 8 steps of intensity from 100 to 5 mW/cm^2. The intensity of the light transmitted through the filter was independently measured by using a power meter. UV-vis absorption spectra were analyzed using a Cary 5000 UV-visible-Near Infrared (UV-vis-NIR) double-beam spectrophotometer. The surface morphology of the polymer layers was characterized using atomic force microscopy (AFM) (Multimode IIIa, Digital Instruments) in a tapping mode, and the bulk morphology was characterized by transmission electron microscopy (TEM) (a Hitachi 7600 operated at 100 kV) and two-dimensional grazing incidence wide-angle X-ray scattering (2D-GIWAXS) (PLS-II 9A U-SAXS beamline, Pohang Accelerator Laboratory; $E_k = 11.24$ keV and $\lambda = 1.103$ Å). The 2D-GIWAXS measurements were carried out with a sample-to-detector separation of 211.23 nm and the angle of incidence of the X-rays was 0.12°. The charge carrier mobility (i.e., electron mobility) was determined by fitting the dark $J - V$ characteristics using the field-independent space-charge limited current (SCLC), where the current density is given by $J = 9\varepsilon_0\varepsilon_r\mu V^2/8L^3 \exp[0.89(V/L)^{0.5}]$, where $\varepsilon_0\varepsilon_r$ is the permittivity of the material, μ is the mobility, and L is the thickness of the polymer layer. The applied bias voltage was corrected for the built-in potential so that $V = V_{applied} - V_{bi}$.

Organic photovoltaic devices can be described using a Shockley equivalent circuit,[15,16] whereby the current density is given by

$$J = \left\{ J_0 \exp(\frac{-\Delta E_{DA}}{2nk_BT}) \left[\exp\left(\frac{q(V - JR_s)}{nk_BT}\right) - 1 \right] + \frac{V}{R_p} \right\} \frac{1}{R_s/R_p + 1} - J_{ph}(V), \quad (1)$$

where V is the applied voltage, ΔE_{DA} is a difference between the donor and acceptor energy levels, n is the ideality factor, k_B is the Boltzmann's constant, J_0 is the reverse saturation current, R_s is the series resistance, and R_p is the shunt resistance. For solar cells with a minimal leakage current (i.e., where $R_p \gg R_s$), Eq. (1) can be simplified to

$$J = \left\{ J_0 \exp(\frac{-\Delta E_{DA}}{2nk_BT}) \left[\exp\left(\frac{q(V - JR_s)}{nk_BT}\right) - 1 \right] + \frac{V}{R_p} \right\} - J_{ph}(V). \quad (2)$$

Under open circuit conditions (i.e., $V = V_{oc}$), there is no output current (i.e., $J = 0$) because the carrier recombination rate becomes equal to the carrier generation rate. Assuming open circuit conditions, a short circuit current of $J_{sc} = J_{ph}(0)$ and a low series resistance, Eq. (2) can be solved to yield the following expression for V_{oc}:[16,17]

$$V_{oc} \approx \frac{nk_BT}{q} \ln(\frac{J_{sc}}{J_o}) + \frac{\Delta E_{DA}}{2q}. \quad (3)$$

To achieve the maximum possible V_{oc} for a given donor/acceptor bilayer, J_0 should be minimized. As discussed above, J_0 is the reverse-bias saturation current, which is the dark current that results from generated thermally carriers at the donor/acceptor interface and in the bulk of the film. For systems where J_0 is dominated by recombination, which is the case for most organic solar cells, J_0 can be expressed as follows:[18]

$$J_0 = J_{oo'} \exp(\frac{-\Delta E_{DA}}{2nk_BT}), \quad (4)$$

where $J_{oo'}$ is a current prefactor which depends on the material properties, including the electrical conductivities of the layers and the molecular structure of the films.[15,18] The terms in this expression that contribute most significantly to the changes in V_{oc} are discussed below.

Figure 1(b) shows $J - V$ curves of inverted P(NDI2OD-T2)/PTB7 bilayer solar cells with P(NDI2OD-T2) layers annealed at different temperatures under illumination. The P(NDI2OD-T2)/PTB7 devices annealed at 100 °C and 150 °C exhibited similar open-circuit voltages of V_{oc} = 0.72 V and V_{oc} = 0.71 V, respectively (see Table I). With the devices annealed at 200 °C for the P(NDI2OD-T2) layer, the open-circuit voltage decreased significantly to V_{oc} = 0.51 V. For the devices annealed at 250 °C, the open-circuit voltage was V_{oc} = 0.77 V.

To investigate how thermal annealing affects V_{oc}, the dark current $J - V$ characteristics were investigated and fitted to Eq. (1) to extract J_0. Values of $J_{oo'}$ were then determined using Eq. (4), which allowed us to calculate the simulated open-circuit voltage V_{oc}^{cal} (see Table II). From these

TABLE I. The performance of inverted bilayer solar cells with annealing temperatures of 100 °C, 150 °C, 200 °C, and 250 °C.

Annealing temperature (°C)	V_{oc} (V)	J_{sc} (mA/cm^2)	FF (%)	PCE (%)	R_pA^a (kΩ cm^2)	R_sA^b (Ω cm^2)
100	0.72	6.0	49.5	2.14	8.12	902.1
150	0.71	5.8	44.5	1.80	7.24	1894.0
200	0.51	5.5	41.2	1.15	5.81	2005.0
250	0.77	5.1	45.3	1.77	10.7	1100.0

[a]Parallel resistance, R_p, is extracted from the near short circuit current.
[b]Series resistance, R_s, is extracted from the near open circuit voltage.

data, we can see that, as the annealing temperature increased to 200 °C, J_0 increased (increasingly markedly at 200 °C); however, V_{oc} exhibited the opposite behavior. These findings indicate that J_0 is important in changing V_{oc}. In addition, as can be seen from Fig. 1(c), the simulated values of V_{oc}^{cal} were consistent with the experimentally measured values of V_{oc} (i.e., V_{oc}^{exp}) (note that differences between V_{oc}^{exp} and V_{oc}^{cal} are due to differences in the current-dependent terms).

The origin of the variation in V_{oc} with the annealing temperature was investigated by measuring the absorption spectra. Figure 1(d) shows UV-vis absorption spectra of the P(NDI2OD-T2) for the different annealing temperatures. The absorption spectra of P(NDI2OD-T2) depended strongly on the annealing temperature and were also shown to be dependent on the molecular conformation. It follows that the optical absorption is a useful property to investigate the aggregation of the P(NDI2OD-T2) molecules and the molecular order. The films that were annealed at 100 °C and 150 °C exhibited similar absorption spectra, whereas the P(NDI2OD-T2) film that was annealed at 200 °C exhibited a strong absorption peak at ~705 nm, with a distinct shoulder feature. This suggests that enhanced stacking occurred inside the P(NDI2OD-T2) phase annealed at 200 °C, which is indicative of strong molecular interactions.[19] Interestingly, however, a further increase in the annealing temperature to 250 °C resulted in a reduction in the optical absorption, which may be due to a loss of order of the P(NDI2OD-T2) phase.

To investigate the morphological properties of the annealed films, we used AFM to characterize the crystallites in the active P(NDI2OD-T2) layer, as shown in Figs. 2(a)–2(d). Annealing at 200 °C resulted in the greatest phase separation, with more aggregation at the surfaces and the largest root-mean-square surface roughness of 0.74 mm, which is attributed to more ordered domains of P(NDI2OD-T2).[20] Upon increasing the annealing temperature to 250 °C, the size of the domains decreased, as did the surface roughness. These trends are consistent with the UV-vis absorption results. We hypothesized that the thermal annealing encourages P(NDI2OD-T2) crystal growth by enhancing the π-π stacking forces, which could lead to an increase in J_0, resulting in a low V_{oc}.

This hypothesis was further examined using 2D-GIWAXS to characterize the structural changes in the P(NDI2OD-T2) films as a function of the annealing temperature, as shown in Figs. 2(e)–2(h). There was a range of diffraction characteristics of the P(NDI2OD-T2) films depending on the process-ing conditions. First, in all of the 2D-GIWAXS patterns, peaks corresponding to (010) π-π interactions were dominant at $q_z \approx 1.58$ Å^{-1} in the out-of-plane direction. These are attributed to the face-on stacking of P(NDI2OD-T2).[21] High crystallinity and ordered packing were evidenced from the strong diffraction peaks, with the film annealed at 200 °C suggesting the greatest degree of order and the

TABLE II. The Shockley parameters for all devices determined by fitting the electrical characteristics in the dark using an equivalent circuit model. V_{oc}^{cal}: Calculated open-circuit voltage. V_{oc}^{exp}: Measured open-circuit voltage.

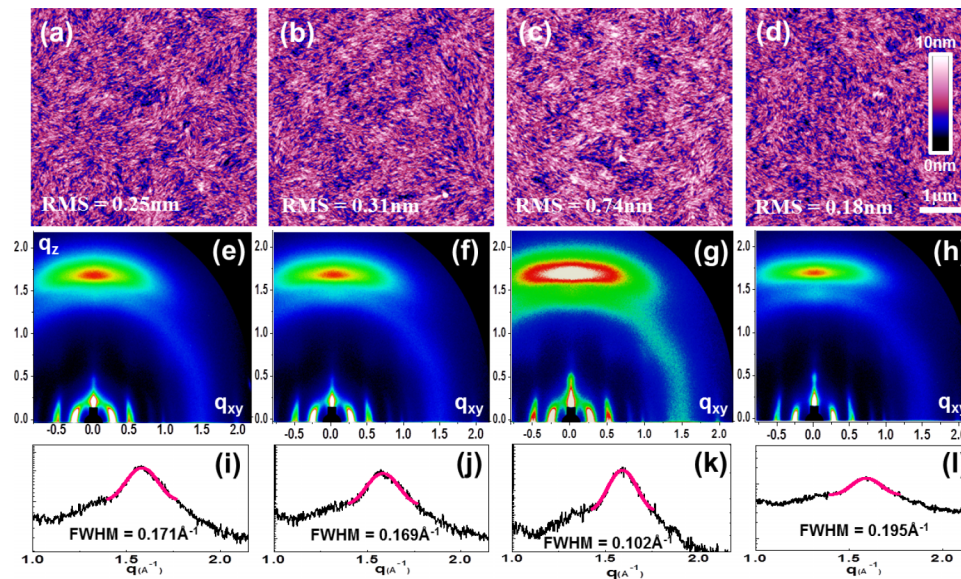| Annealing temperature (°C)	n	J_0 (A/cm^2)	$J_{oo'}$ (A/cm^2)	$nk_BT/q \ln(J_{sc}/J_o)$	$\Delta E_{DA}/2q$	V_{oc}^{cal} (V)	V_{oc}^{exp} (V)
100	1.87	2.63×10^{-9}	1.89×10^{-4}	0.163	0.564	0.727	0.720
150	1.90	2.92×10^{-9}	2.13×10^{-4}	0.158	0.564	0.722	0.714
200	2.02	1.86×10^{-7}	1.31×10^{-2}	−0.045	0.564	0.519	0.516
250	1.93	1.27×10^{-9}	9.86×10^{-5}	0.202	0.564	0.766	0.771

FIG. 2. First row: surface morphologies of the P(NDI2OD-T2) layers measured using AFM. Second row: 2D-GIWAXS patterns of the P(NDI2OD-T2) films annealed at different temperatures. Third row: out-of-plane scattering profiles of the (010) peak position along the q_z-axis fitted using a Gaussian model. ((a), (e), and (i)) 100 °C, ((b), (f), and (j)) 150 °C, ((c), (g), and (k)) 200 °C, and ((d), (h), and (l)) 250 °C.

film annealed at 250 °C the least. We calculated the domain size of the P(NDI2OD-T2) crystallites using the Scherrer equation,[22] i.e., $\tau = 0.9\lambda/\beta\,(\mathrm{FWHM})\cos\theta$, where τ is the mean size of the ordered crystalline domains, λ is the X-ray wavelength, and β is the line broadening at the full width at half maximum (FWHM). The (010) peak positions and FWHMs of the samples were extracted using Gaussian fitting to the detailed interference profiles along the out-of-plane directions, as shown in Figs. 2(i)–2(l). As expected, τ was larger for the samples with a higher degree of crystallinity; we found that $\tau = 58.9$ Å for the sample annealed at 100 °C, $\tau = 59.3$ Å for the sample annealed at 150 °C, $\tau = 98.7$ Å for the sample annealed at 200 °C, and $\tau = 51.4$ Å for the sample annealed at 250 °C. These data on the physical characteristics of the acceptor films as a function of annealing temperature provide useful information on the crystallinity, crystal structure, and the packing ordering; furthermore, these properties were strongly correlated with the UV-vis absorption spectra and the AFM data. From this 2D-GIWAXS analysis, we may conclude that the thermal annealing conditions significantly affected the P(NDI2OD-T2) crystalline structure, and that more ordered π-π packing morphologies and larger crystallite sizes corresponded to larger values of J_0. Accordingly, this is one of the first examples showing the correlation between crystalline domains and the saturation dark current in bilayer APSCs.

Additionally, to clearly confirm that whether there is a change in PTB7 layers by P(NDI2OD-T2) bottom films with different conditions, we investigated the surface and bulk morphology of PTB7 layers using AFM and TEM techniques, respectively (Fig. 3). All four PTB7 films showed quite similar morphologies in both surface and bulk states: the fine features of a homogeneous phase without any coarsened separated domains. These results indicate that there are no direct effect on the top layers, PTB7 layers, by bottom films treated with different thermal annealing, and thus, we could claim that our concept is distinctly due to the morphological change of P(NDI2OD-T2) bottom layers.

To obtain further insight into the influence of the P(NDI2OD-T2) crystalline domains on the charge transport properties, the charge carrier (electron) mobility was measured using a SCLC method with an n-type Al/P(NDI2OD-T2)/Al device structure. Based on Equation (4) and the curves shown in Fig. 4(a), we calculated the following electron mobilities: 2.31×10^{-3} cm^2 V^{-1} s^{-1} (P(NDI2OD-T2) thickness: 41 ± 0.5 nm) for the device annealed at 100 °C, 2.17×10^{-3} cm^2 V^{-1} s^{-1} (P(NDI2OD-T2) thick-
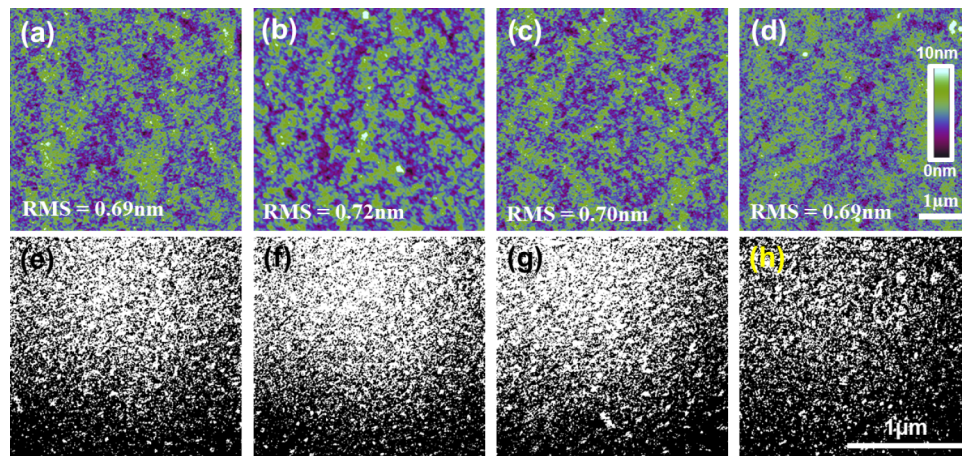
FIG. 3. AFM height images of the PTB7 layers (upper panel) and TEM images of top layers (lower panel) spin-coated on the P(NDI2OD-T2) films treated with thermal annealing at ((a) and (e)) 100 °C, ((b) and (f)) 150 °C, ((c) and (g)) 200 °C, and ((d) and (h)) 250 °C.

ness: 40 ± 0.7 nm) for the device annealed at 150 °C, 9.82×10^{-3} cm^2 V^{-1} s^{-1} (P(NDI2OD-T2) thickness: 42 ± 0.2 nm) for the device annealed at 200 °C, and 9.67×10^{-4} cm^2 V^{-1} s^{-1} (P(NDI2OD-T2) thickness: 41 ± 0.6 nm) for the device annealed at 250 °C. These should be significantly responsible for above morphological results by AFM and 2D-GIWAXS. In other words, a higher electron mobility can be expected in more ordered P(NDI2OD-T2) crystalline domains,[23] which is consistent with the measured data on crystalline quality.

In general, V_{oc} is determined by a trade-off between recombination and generation of charge carriers. It has been reported that recombination (particularly bimolecular recombination) is related to J_0 and is the dominant recombination loss mechanism in organic solar cells under open-circuit
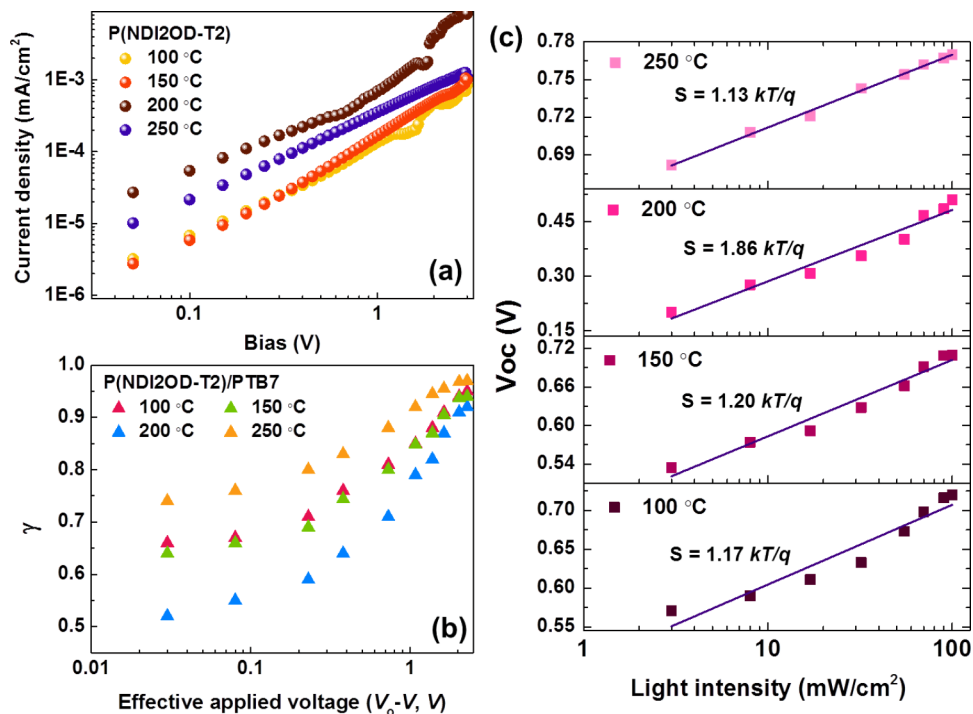

FIG. 4. (a) $J-V$ plots of the n-type devices. (b) The exponent γ as a function of the effective applied voltage. (c) The photovoltage as a function of the intensity of the incident light for APSCs with different annealing temperatures.

conditions.[24] To investigate the difference in bimolecular recombination between P(NDI2OD-T2) AP-SCs annealed at different temperatures, independent measurements of the light-intensity-dependent steady-state photocurrent were carried out. The recombination parameter γ can be obtained by fitting to $J_{ph} \approx I(light\ intensity)^\gamma$.[25] Fig. 4(b) shows the fitting exponent γ as a function of effective applied voltage, i.e., V_0–V, where V_0 corresponds to V_{oc} at $J_{ph} = 0$, and V is the applied bias (note that a larger γ corresponds to less bimolecular recombination[24]). These data show that the device annealed at 250 °C exhibited the largest value of γ, and the device annealed at 200 °C exhibited the smallest. These data suggest that thermal motion during annealing allows crystallization of the P(NDI2OD-T2) phase, leading to increased bimolecular recombination, and thus a decrease in V_{oc} with increasing J_0 (i.e., dark current). Therefore, the low value of $V_{oc} = 0.51$ V for the P(NDI2OD-T2)/PTB7 device annealed at 200 °C results from increased bimolecular recombination, and hence a larger J_0.

The recombination mechanisms were investigated by studying V_{oc} as a function of the charge carrier generation rate, which was varied by controlling the intensity of the incident light. The slope of V_{oc} as a function of the log of the optical intensity allows us to determine the degree of trap-assisted recombination. A slope of $k_B T/q$ implies that bimolecular recombination is the dominant mechanism, where q is the electronic charge.[26] With trap-assisted recombination, a stronger dependence of V_{oc} on the optical intensity with a slope of 2 kT/q is observed.[26,27] As shown in Fig. 4(c), the inverted P(NDI2OD-T2)/PTB7 devices (except for that annealed at 200 °C) exhibited similar slopes, which were indicative of bimolecular recombination (i.e., $kT/q = 1.17$ at 100 °C, $kT/q = 1.20$ at 150 °C, and $kT/q = 1.13$ at 250 °C), whereas we found that $kT/q = 1.86$ for the device annealed at 200 °C. These results indicate that highly ordered P(NDI2OD-T2) layers annealed at 200 °C with large crystalline domains exhibited increased interfacial surface trap densities between the active layers, which resulted in elevated trap-assisted recombination in combination with bimolecular recombination, leading to a large J_0.

In summary, we fabricated bilayer all-polymer P(NDI2OD-T2)/PTB7 solar cells with an inverted configuration, where the annealing temperature was systematically varied. The size of the crystalline domains of the P(NDI2OD-T2) depended on the annealing temperature, and variations in the photovoltage are attributed to differences in the morphological packing structure of the P(NDI2OD-T2) layer. Layers with more ordered and larger crystallites resulted in increased trap-assisted recombination rates, as well as increased bimolecular recombination rates, resulting in large saturation dark current density, J_0, and thus a small V_{oc}. This work may therefore serve as a guide to the process conditions for P(NDI2OD-T2) layers in all-polymer solar cells.

[1] N. Zhou, H. Lin, S. J. Lou, X. Yu, P. Guo, E. F. Manley, S. Loser, P. Hartnett, H. Huang, M. R. Wasielewski, L. X. Chen, R. P. H. Chang, A. Facchetti, and T. J. Marks, Adv. Energy Mater. **4**, 1300785 (2014).

[2] K. D. Deshmukh, T. Qin, J. K. Gallaher, A. C. Y. Liu, E. Gann, K. O'Donnell, L. Thomsen, J. M. Hodgkiss, S. E. Watkins, and C. R. McNeill, Energy Environ. Sci. **8**, 332 (2015).

[3] J. W. Jung, J. W. Jo, C.-C. Chueh, F. Liu, W. H. Jo, T. P. Russell, and A. K.-Y. Jen, Adv. Mater. **27**, 3310 (2015).

[4] C. Lee, H. Kang, W. Lee, T. Kim, K.-H. Kim, H. Y. Woo, C. Wang, and B. J. Kim, Adv. Mater. **27**, 2466 (2015).

[5] Y. Zhou, T. Kurosawa, W. Ma, Y. Guo, L. Fang, K. Vandewal, Y. Diao, C. Wang, Q. Yan, J. Reinspach, J. Mei, A. L. Appleton, G. I. Koleilat, Y. Gao, S. C. B. Mannsfeld, A. Salleo, H. Ade, D. Zhao, and Z. Bao, Adv. Mater. **26**, 3767 (2014).

[6] T. Earmme, Y.-J. Hwang, S. Subramaniyan, and S. A. Jenekhe, Adv. Mater. **26**, 6080 (2014).

[7] L. Huo, T. Liu, X. Sun, Y. Cai, A. J. Heeger, and Y. Sun, Adv. Mater. **27**, 2938 (2015).

[8] C.-C. Chen, W.-H. Chang, K. Yoshimura, K. Ohya, J. You, J. Gao, Z. Hong, and Y. Yang, Adv. Mater. **26**, 5670 (2014).

[9] B. Burkhart, P. P. Khlyabich, and B. C. Thompson, Macromolecules **45**, 3740 (2012).

[10] C. Poelking, M. Tietze, C. Elschner, S. Olthof, D. Hertel, B. Baumeier, F. Würthner, K. Meerholz, K. Leo, and D. Andrienko, Nat. Mater. **14**, 434 (2015).

[11] Z. Wang, Y. Uemura, Y. Zhoum, T. Miyadera, R. Azumi, Y. Yoshida, and M. Chikamatsu, ACS Appl. Mater. Interfaces **7**, 10814 (2015).

[12] M. D. Perez, C. Borek, S. R. Forrest, and M. E. Thompson, J. Am. Chem. Soc. **131**, 9281 (2009).

[13] B. Kitchen, O. Awartani, R. J. Kline, T. McAfee, H. Ade, and B. T. O'Connor, ACS Appl. Mater. Interfaces **7**, 13208 (2015).

[14] Y. Sun, J. H. Seo, C. J. Takacs, J. Seifter, and A. J. Heeger, Adv. Mater. **23**, 1679 (2011).

[15] J. H. Lee, S. Cho, A. Roy, H.-T. Jung, and A. J. Heeger, Appl. Phys. Lett. **96**, 163303 (2010).

[16] B. Rand, D. Burk, and S. Forrest, Phys. Rev. B: Condens. Matter Mater. Phys. **75**, 115327 (2007).

[17] Z. Yi, W. Ni, Q. Zhang, M. Li, B. Kan, X. Wan, and Y. Chen, J. Mater. Chem. C **2**, 7247 (2014).

[18] P. Würfel, *Physics of Solar Cells: From Principles to New Concepts* (Wiley-VCH, Weinhem, 2005).

[19] N. M. Murari, M. J. Crane, T. Earmme, Y.-J. Hwang, and S. A. Jenekhe, Appl. Phys. Lett. **104**, 223906 (2014).

[20] Y. Liu, J. Zhao, Z. Li, C. Mu, W. Ma, H. Hu, K. Jiang, H. Lin, H. Ade, and H. Yan, Nat. Commun. **5**, 5293 (2014).

[21] Y. J. Kim, D. S. Chung, and C. E. Park, Nano Energy **15**, 343 (2015).

[22] P. Müller-Buschbaum, Adv. Mater. **26**, 7692 (2014).

[23] J. Seifter, Y. Sun, H. Choi, B. H. Lee, T. L. Nguyen, H. Y. Woo, and A. J. Heeger, Adv. Mater. **27**, 4989 (2015).

[24] B. Yang, Y. Yuan, and J. Huang, J. Phys. Chem. C **118**, 5196 (2014).

[25] C. M. Proctor and T.-Q. Nguyen, Appl. Phys. Lett. **106**, 083301 (2015).

[26] L. J. A. Koster, V. D. Mihailetchi, R. Ramaker, and P. W. M. Blom, Appl. Phys. Lett. **86**, 123509 (2005).

[27] L. Lu, W. Chen, T. Xu, and L. Yu, Nat. Commun. **6**, 7327 (2015).